

See discussions, stats, and author profiles for this publication at: <https://www.researchgate.net/publication/263961437>

# Hierarchical Multiscale Modeling of Polymer–Solid Interfaces: Atomistic to Coarse-Grained Description and Structural and Conformational Properties of Polystyrene–Gold Systems

ARTICLE *in* MACROMOLECULES · JULY 2013

Impact Factor: 5.8 · DOI: 10.1021/ma400357r

---

CITATIONS

18

---

READS

12

## 2 AUTHORS:



[Karen Johnston](#)

University of Strathclyde

30 PUBLICATIONS 621 CITATIONS

SEE PROFILE



[V. A. Harmandaris](#)

University of Crete

59 PUBLICATIONS 1,900 CITATIONS

SEE PROFILE

# Hierarchical Multiscale Modeling of Polymer–Solid Interfaces: Atomistic to Coarse-Grained Description and Structural and Conformational Properties of Polystyrene–Gold Systems

Karen Johnston<sup>\*,†</sup> and Vagelis Harmandaris<sup>‡,§</sup>

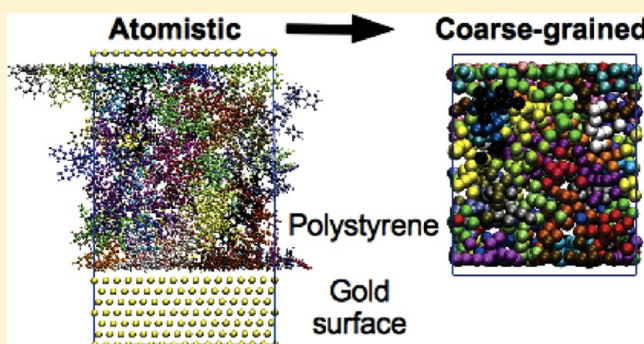
<sup>†</sup>Max Planck Institute for Polymer Research, Ackermannweg 10, 55128 Mainz, Germany

<sup>‡</sup>Department of Applied Mathematics, University of Crete, GR-71409 Heraklion, Crete, Greece

<sup>§</sup>IACM FORTH, GR-71110 Heraklion, Crete, Greece

## S Supporting Information

**ABSTRACT:** A hierarchical simulation approach was developed in order to study polystyrene films sandwiched between two parallel Au(111) surfaces. The coarse-grained potentials describing the interaction of polystyrene with the gold surface were developed systematically using constrained all-atom molecular simulations of a styrene trimer on the Au(111) surface. The model was validated by studying a 5 nm film of short (10-mer) atactic polystyrene chains using all-atom and coarse-grained molecular dynamics simulations. The density, structure, and conformational properties of coarse-grained films were found to be in excellent agreement with all-atom ones. The coarse-grained model was then used to study the structural and conformational properties of roughly 10 and 20 nm thick films with 10-, 50-, 100-, and 200-mer chains. The width of the interphase region of the polymer films is property specific. The density profiles reached the bulk value around 1.5 nm from the interface, for all chain lengths. An estimate of the width of the interphase region based on the conformation tensor profile indicates that the interphase width is around 2–3 times the radius of gyration, which is proportional to the square root of the chain length (number of monomers), and for 200-mer chains is approximately 6–10 nm.



## INTRODUCTION

Polymer thin films are encountered in a variety of different technological applications including adhesives, paint, lubricants, and multiphase composite materials. The overall performance of such materials depends on the polymer properties close to the interface. Nowadays, the design of functional materials used in different applications, such as organic electronics or miniaturized devices, often involves polymer–solid interfaces.<sup>1,2</sup> Because of this broad spectrum of technological applications, the properties of polymer–solid interfaces are a very intense research field. Various experimental approaches have been used to study the structural and dynamical properties at a solid surface.<sup>3–6</sup> In addition, a range of simulation methodologies have been employed to study the effect of the interface on the polymer properties. The challenge in simulating these systems is the large range of time and length scales involved, and a multiscale modeling approach is necessary. This is an inherent problem in all macromolecular materials since it is related to the different characteristic time scales associated with the motion of different parts of the chain from femtoseconds for bond vibrations up to seconds for long polymer chain relaxations near the glass transition temperature.<sup>7</sup>

Atomistic simulations have the advantage of a detailed all-atom representation of the hybrid material, and therefore, a direct quantitative comparison can be made between the predicted properties and experimental quantities.<sup>8–10</sup> However, the main problem related with the application of atomistic techniques on polymeric materials is the long relaxation times required for equilibration. For polymer–solid systems even longer time scales are involved due to the presence of the solid surface, which might slow the polymer dynamics even further.<sup>8,11–14</sup> In order to reach longer simulation times, systematic coarse-grained models have been developed for various macromolecules,<sup>15–17</sup> where the main idea behind such models is to group chemically connected atoms into “superatoms” or “beads” and derive the effective CG interaction potential (free energy) by taking into account the atomistic details of the particular polymer. The CG model developed for bulk polystyrene,<sup>17</sup> which we use in this work, has been shown to give a speed up of around 3 orders of magnitude compared to AA simulations.<sup>18</sup> This speedup is due to a couple of

**Received:** February 20, 2013

**Revised:** June 24, 2013

**Published:** July 2, 2013

different factors: first, the calculation is faster due to fewer particles and interactions, and second, the CG dynamics is faster due to the lower frictional forces of the smoother potentials. To date, there are only a few systematic CG studies of polymer–solid systems. For example, the interaction of polycarbonate near a solid surface has been studied by combining *ab initio* calculations, describing the interaction of fragments of the polymer with the surface, with CG molecular dynamics.<sup>19,20</sup>

The present work is a part of a systematic approach that hierarchically links together different levels of description starting from the quantum level through the atomistic level and to the coarse-grained level. Our primary goal is to study a realistic polymer–solid interfacial system and predict its properties directly from the molecular structure. In previous work, we studied polystyrene–gold systems using atomistic simulations, where the interface potentials were obtained from density functional theory (DFT) calculations of small PS fragments. The adsorption energy of the fragments on a gold surface as a function of distance from the surface for various adsorption sites and molecular orientations<sup>14,21</sup> was used to parametrize a classical force field for the PS–Au interaction that describes accurately all the DFT data. In this work we systematically derive a CG potential for the PS–Au interface and use it to model PS chains with larger molecular weight. We start by developing coarse-grained surface potentials, which are based on the atomistic sampling of oligomers on the surface. The CG potentials are then validated by comparing atomistic and coarse-grained simulations of a short-chain polystyrene melt on gold. Finally, systems with longer-chain polymers are investigated, and density profiles, structures, and conformations of such systems are analyzed.

## METHOD

The proposed methodology involves the development of a rigorous CG PS–Au interaction potential based on atomistic (AA) data, which were in turn based on DFT calculations.<sup>14,21</sup> All AA and CG simulations were performed using GROMACS 4.5.<sup>22</sup> Details about the atomistic simulations and force field can be found elsewhere.<sup>14,23</sup> For this study a previously developed CG model for PS was used.<sup>17,24</sup> In this model a monomer is represented by two beads, which we denote E (the ethylene backbone group) and P (the phenylene side group) (see Figure 1). This model is capable of describing quantitatively the structure, dimensions, and conformations of PS chains in the bulk. Here, we extend this model in order to describe the PS–Au interaction. In the present case, the CG systems consist of five different atactic chain types, e.g., a 50-chain system has 10 chains of each chain type. The bulk CG systems were set up by placing linear polymer chains in a large hexagonal box with vectors  $\mathbf{a} = a\hat{i}$ ,  $\mathbf{b} = a(-\frac{1}{2}\hat{i} + \frac{\sqrt{3}}{2}\hat{j})$ , and  $\mathbf{c} = c\hat{k}$ . The chains were relaxed using energy minimization and soft-core potentials, followed by an NpT simulation with  $p = 1$  atm and  $T = 500$  K, using the Berendsen barostat and stochastic velocity rescaling thermostat,<sup>25</sup> until the bulk density was reached. The box was fixed in  $x$  and  $y$  and allowed to vary only along  $z$ .

For the simulations of 10-mer PS on Au the simulation boxes were hexagonal with  $a = b = 4.616$  nm, corresponding to  $16 \times 16$  surface unit cells. For the longer chain systems a larger surface was used so that the sides of the simulation cell were all longer than the ensemble averaged end-to-end distances. For the 50-, 100-, and 200-mer systems  $a = 6.347$ ,  $9.232$ , and  $12.694$  nm, respectively. These lengths are integer multiples of

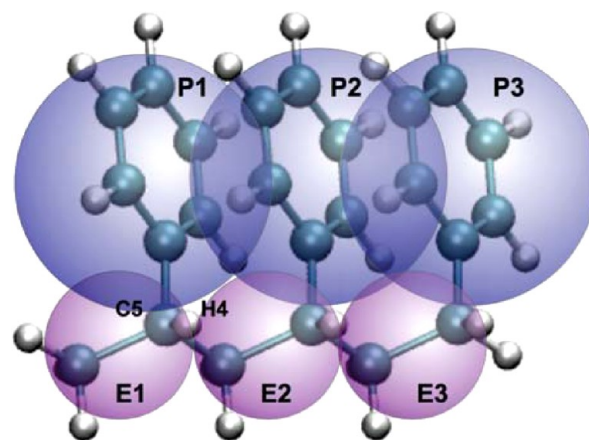


**Figure 1.** CG bead labeling for surface interaction of a PS isotactic trimer. Atoms C5 and H4 in the picture belong to E1 in the surface interaction.

the surface unit cell of gold, which is important so that the CG system can later be backmapped back to the atomistic system. The surface interaction is set up using wall potentials at the bottom and top of the box in  $z$ -direction and periodic boundary conditions in the  $xy$ -plane. A time step of 1 fs was used for all systems unless otherwise stated. The 10-mer systems were equilibrated by running the simulations until the bulk density is reached and then allowing the end-to-end vectors to decorrelate before taking statistics. Equilibration of long polymer chains is a nontrivial issue, and this will be discussed in a later section.

If we were interested in obtaining the effective CG interaction between a simple molecule (e.g., benzene) and a solid surface, then we would directly calculate the potential of mean force (PMF) between the molecule and the solid surface. However, for the case of a macromolecular chain we must consider the fact that the CG bead belongs in a polymer chain, and indeed, the set of the allowed conformations will be different in the latter case. Therefore, to mimic the polymer chain, we calculate the PMF for the CG beads using a PS oligomer. The CG PS–Au interactions for each bead type must be developed independently. The bead types are shown in Figure 1 and are described in more detail in the Supporting Information.

At the coarse-grained level the interaction between the polystyrene and the surface is represented by a  $z$ -dependent wall potential. Clearly, this approach neglects the structure of the surface; however, in the case of the Au(111) surface the site dependence of the PS–Au interaction is rather weak,<sup>14</sup> which to an extent justifies this approach. Nevertheless, the frictional properties of the surface will be different, which will affect the dynamical behavior of the polymer at the surface. This will be the subject of a future study.

For the effective potential calculations we used a procedure based on a single PS oligomer near the surface. A similar method was used previously in a study of bulk PS in order to develop the nonbonded CG interaction between CG beads in the bulk.<sup>17</sup> For the bulk case, the effective interaction between the two CG beads at a fixed distance,  $r$ , was computed via the constraint force required to keep the two CG beads at this specific distance. In the present case, a single PS oligomer is placed near the gold surface and the system is run, keeping the center of mass of the group of interest fixed at a particular

distance,  $z$ , from the surface. The group was placed every 0.05 nm in the range  $z_1 = 0.25$  nm up to  $z_2 = 1.5$  nm, and each simulation was run for 10 ns with output every 0.1 ps. The average constraint forces,  $f_c$ , were integrated using the trapezium rule to give the PMF

$$V_{\text{PMF}}(z) = - \int_{z_1}^{z_2} [\langle f_c \rangle_z] dz \quad (1)$$

The simulation is repeated, using the same trajectory file, with the interactions between the constrained group and the surface atoms turned off to obtain  $V_{\text{PMF,excl}}(z)$ . The effective potential for the constrained group with the surface is obtained by subtracting the excluded-interaction PMF from the full-interaction PMF

$$V_{\text{eff}}(z) = V_{\text{PMF}}(z) - V_{\text{PMF,excl}}(z) \quad (2)$$

## DEVELOPMENT OF THE COARSE-GRAINED POLYMER–SURFACE POTENTIALS

In this part we describe the development of the interaction potential between the CG beads and the Au solid layers as a function of the length of the PS oligomer. We further study the effect of tacticity on the derived potential by using pure stereoregular (isotactic and syndiotactic) PS sequences. Note that the PS–Au interaction developed here includes entropic (temperature) effects as all interactions in the CG description are derived from PMFs (free energies). This is in contrast with CG potentials developed in the past using ab initio data, which are based on the ground state (zero temperature) potential energy.<sup>19,20</sup> The latter approach is expected to be a reasonable approximation of the interface potential as long as the CG superatom–surface interaction is enthalpy dominated, i.e., very strong compared to the thermal energy. The current approach explicitly accounts for entropy, which is expected to be very important for soft matter systems, thus being applicable to all soft–hard matter interfaces.

**Effect of the Oligomer Length.** The first issue to be addressed is the length of the oligomer necessary to obtain realistic sampling of the allowed conformations. To determine this, we calculated effective potentials using a 3-mer, a 5-mer, and a 7-mer for an isotactic chain. The beads at the chain ends will not interact with the surface in the same way as those in the middle of the chain, and it is important to differentiate between these beads. Since the central beads are more likely to be affected by the surrounding chain, we have considered the central beads rather than the beads at the chain ends. The results for isotactic 3-, 5-, and 7-mer chains are shown in Figure 2.

The effective potentials for the central E bead are shown in Figure 2a. Clearly for the three different chain lengths the potentials are very similar. Therefore, we can conclude that the 3-mer is sufficient for sampling the conformational space of the E beads.

The case of the P beads is different. The effective potentials for the central phenylene bead in each oligomer is shown in Figure 2b. There is a small difference in the shape of the three curves around 0.35 nm from the surface. To check that this is not due to poor sampling, the calculations in the range 0.3–0.4 nm were extended to 100 ns, and the results were very similar. Hence, this effect is likely to be due to long-range correlations in the chain. This is not surprising if we consider that for the CG model it was necessary to take 1–5 interactions into

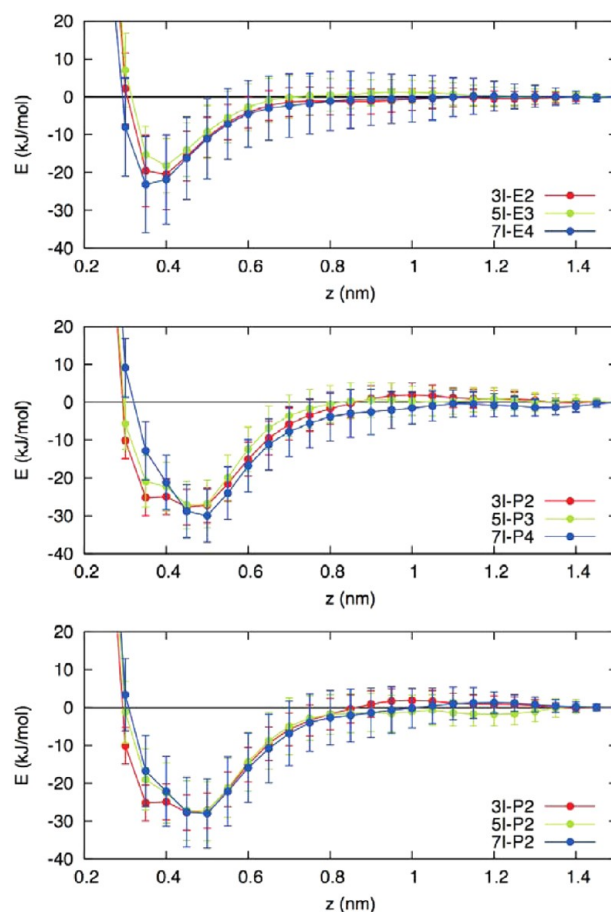


**Figure 2.**  $V_{\text{eff}}(z)$  for (a) the central E bead, (b) the central P bead, and (c) the second P bead (P2) in 3-mer, 5-mer, and 7-mer isotactic (I) oligomers.

account to obtain the correct local structure of the bulk PS chains. The shorter oligomers are missing the long-range interactions which may result in different conformations with lower energy around 0.35 nm. To further check that this is the likely explanation,  $V_{\text{eff}}$  for the second phenylene bead (P2) in each oligomer was calculated. In the 5-mer and 7-mer chains the P2 bead has the same interactions up to the sixth nearest neighbor, compared to only the fourth nearest neighbor for the central bead. The effective potentials for the P2 bead are shown in Figure 2c, and  $V_{\text{eff}}$  for the 5-mer and 7-mer agree.

**Effect of Tacticity and Chain Ends.** Next we consider the effect of tacticity and bead position. This is particularly important if we consider that our PS CG model has the advantage of describing accurately the tacticity of PS bulk systems. Therefore, we would also like to calculate the PS/Au interaction for isotactic and syndiotactic PS chains.  $V_{\text{eff}}(z)$  for all six beads in isotactic and syndiotactic trimers are shown in Figure 3, and the bead labeling is shown in the inset of Figure 3a. All the ethylene beads have very similar effective potentials, as seen in Figure 3, and are only weakly dependent on tacticity and position. The strength of the interaction is around 20 kJ/mol, which is lower than the minimum energy of the vertical (27 kJ/mol) and horizontal (35 kJ/mol) configurations calculated using density functional theory.<sup>14</sup> The small difference is not surprising if we consider that the effective potentials explicitly incorporate thermal energy effects.



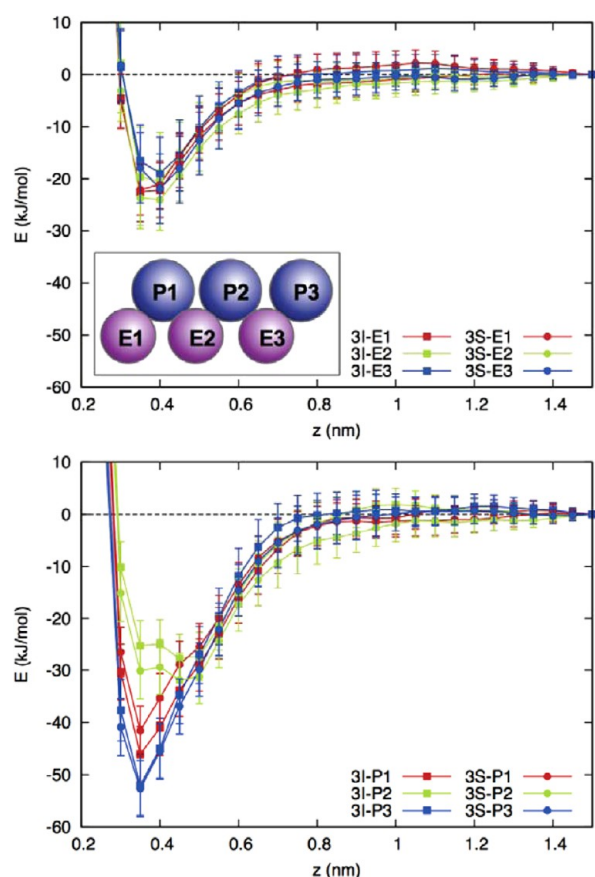


**Figure 3.**  $V_{\text{eff}}(z)$  for (a) the ethylene beads and (b) the phenylene beads in an isotactic (I) and a syndiotactic (S) 3-mer.

There is a clearer difference between the effective potentials for the phenylene beads. The phenylene ring at the end of the chain (P3) is independent of tacticity since the ring is free to rotate or exchange positions with the hydrogen atom. It has the strongest attraction of around 50 kJ/mol due to the fact that it has fewer conformational constraints than more central beads. The phenyl bead at the other end of the chain (P1) experiences some conformational constraints due to the end ethylene bead (E1) and therefore has a slightly weaker interaction of around 45 kJ/mol. The central bead (P2) is the most weakly attractive with an interaction of around 30 kJ/mol. The P1 and P2 beads exhibit only a small dependence on tacticity, which can be neglected.

We can further compare the  $V_{\text{eff}}(z)$  curves with the interaction of benzene on a gold surface.<sup>21</sup> For benzene in a horizontal orientation the minimum energy is around 80 kJ/mol at distance of around 0.3 nm from the surface. The vertical configuration has a weaker interaction of around 30 kJ/mol at a distance of 0.5 nm. As expected, the effective potentials of the phenylene beads represent an average of these orientations due to thermal fluctuations. The chains ends are less constrained and, therefore, more likely to be in a horizontal orientation with a minimum energy around 0.35 nm from the surface. The central beads have more vertical or intermediate orientations with shallower minima further from the surface at around 0.45 nm.

A surface interaction of  $\approx 30$  kJ/mol corresponds to  $7.2kT$  at  $T = 500$  K, which implies that once a bead becomes attached to the surface it remains at the surface for a long time. The bead–surface interactions are considerably stronger than the bead–

bead nonbonded interactions within the bulk polymer. For the bulk polymer the nonbonded potentials are less than 3 kJ/mol deep, which is an order of magnitude weaker than the surface potentials. However, the surface potentials represent the interaction between the bead and many surface atoms, whereas the nonbonded potentials describe individual bead–bead interactions.

**Fitting the Potentials.** For the E beads the effective potentials are very similar, and we have chosen to represent all the E interactions with the same  $V_{\text{eff}}$  namely the isotactic 3-mer for the E2 bead. For the P beads it is clear that the interactions of the chain ends must be treated separately from the central beads, and therefore, we have three different interactions for the P beads: P1 and P3 for the first and last P bead in each chain, respectively, and P2 (or P4 in the case of the 7-mer) for all the others. Since the P1 and P3 beads do not depend much on tacticity, we use the isotactic 3-mer effective potentials for these beads. For the P2 bead it is not *a priori* clear whether it is best to use the 3-mer or 7-mer  $V_{\text{eff}}$  for the P2 bead (again we chose the isotactic chain), although the differences in the effective potentials are small and well within the expected error for CG simulations. Nevertheless, we decided to check whether the properties of the CG system depend on this choice. We also considered whether a simple analytical potential could be used to fit the original  $V_{\text{eff}}$  data or whether a numerical fit was necessary. For the analytic potential we used a Morse-type potential of the form

$$V(z) = \varepsilon \{ \exp[-2\alpha(z - z_0)] - 2 \exp[-\alpha(z - z_0)] \} \quad (3)$$

where  $z$  is the distance to the surface and  $\alpha$ ,  $z_0$ , and  $\varepsilon$  are adjustable parameters. This analytic form was chosen because it was found to accurately describe the atomistic interface pair potentials for the PS–Au AA model systems.<sup>14,21</sup> The parameters that gave the best fit for the CG effective potentials are listed in Table 1.

**Table 1.** Morse Parameters for Each Bead Type in an Isotactic 3-mer<sup>a</sup>

	$\varepsilon$	$z_0$	$\alpha$
3I-E2	20.22	0.3774	9.09
3I-P1	47.00	0.3638	7.73
3I-P2	31.90	0.3913	7.19
3I-P3	51.90	0.3491	8.47

<sup>a</sup> $V_{\text{eff}}$  for the E2 bead in an isotactic 3-mer was used for all E beads.

The effective potential data and fitted potentials are shown in Figure 4. For the P2 bead we show both the 3-mer and 7-mer effective potentials, the cubic spline fits to the 3-mer and 7-mer, and the Morse fit to the 3-mer. It is clear that the Morse potential provides very good fits for the interaction between E, P1, and P3 beads and the Au surface, which all have a clear minimum. However, for the P2 bead in the 3-mer the minimum has a shoulder around 0.35 nm and the Morse potential does not represent this very well. Therefore, all the  $V_{\text{eff}}$  curves were also fit using cubic splines (CS), implemented using the ALGLIB package.<sup>26</sup> The CS fitted potentials were then used in tabulated form. The sensitivity of the results to these three different sets of CG interface potentials is investigated in the following section. The sets are denoted as follows: (a) M-3I-P2: Morse fits for the four bead types in an isotactic 3-mer, (b) CS-3I-P2: CS fits for the four bead types in an isotactic 3-mer, and

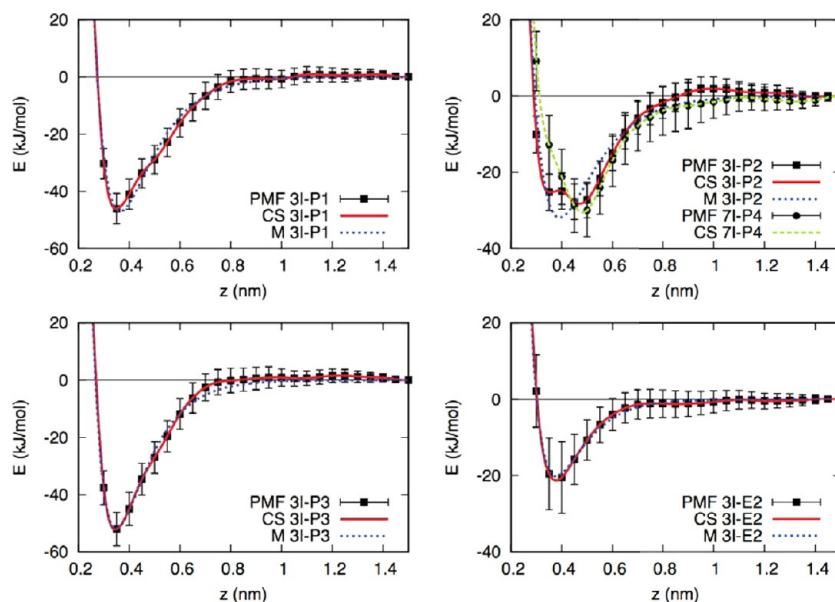


**Figure 4.** Effective potentials, fitted cubic splines, and fitted Morse potentials for the four different CG bead types in an isotactic chain: (a) 3I-P1, (b) 3I-P2 and 7I-P4, (c) 3I-P3, and (d) 3I-E2.

(c) CS-7I-P4: CS fits for E, P1, and P3 in an isotactic 3-mer and P4 (for the central P beads) in an isotactic 7-mer.

## COMPARISON BETWEEN ALL-ATOM AND COARSE-GRAINED SIMULATIONS

To ensure that the CG model and potentials represent the system accurately, we begin with a detailed comparison of a short chain PS/Au system, which can be simulated using both CG and all-atom (AA) models. We chose a 5 nm 10-mer atactic PS/Au film, denoted S5-10, which was previously studied using all-atom MD simulations.<sup>4</sup> For the CG S5-10 systems a time step of 3 fs was used, which did not result in any significant difference from using a time step of 1 fs. A snapshot for this system is shown in Figure 5.

The averaged film properties for the S5-10 system, as well as the bulk systems, using the three different sets of potentials are given in Table 2. Both bulk systems and film contained 50 chains. For the CG bulk 10-mer system the ensemble-averaged chain dimensions are  $\langle R_g \rangle = 0.62$  nm and  $\langle R_e \rangle = 1.55$  nm. To compare the CG system with the AA system, we mapped the

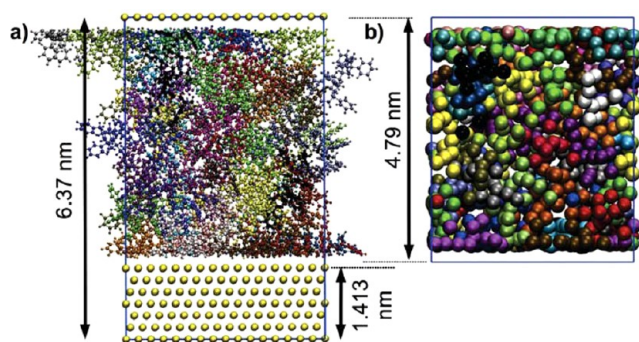


**Figure 5.** Snapshots of the CG S5-10 system with (a) AA and (b) CG (using the 3I-P2 potential) representations. Each chain is represented with a different color. The average box lengths for the AA and CG (3I-P2) systems are 6.37 and 4.79 nm. In the AA case this corresponds to a film thickness of  $\langle L_z \rangle = 4.96$  nm.

**Table 2.** Summary of the 10-mer Film and Bulk Systems Studied, the CG Surface Potentials Used, and the Average Properties<sup>a</sup>

model	label	fit	potential	$\langle L_z \rangle$	$\langle \rho \rangle$	$\langle R_e \rangle$	$\langle R_g \rangle$
AA	B-10				0.97	1.57	0.63
CG	B-10				0.97	1.55	0.62
AA	S5-10			4.96	0.95	1.59	0.63
CG	S5-10	CS	3I-P2	4.79	0.98	1.65	0.63
CG	S5-10	CS	7I-P4	4.75	0.99	1.67	0.63
CG	S5-10	M	3I-P2	4.76	0.98	1.63	0.63

<sup>a</sup>The film thickness,  $L_z$ , and characteristic chain lengths,  $R_e$  and  $R_g$ , are in nm, and the density,  $\rho$ , is in  $\text{g cm}^{-3}$ . The standard deviations of  $R_e$  and  $R_g$  are approximately 0.4 and 0.05 nm in all cases, respectively.

AA system to a CG representation and analyzed this in the same way as the CG systems.  $R_e$  shows the same trend for the AA and CG systems; that is, the S5-10 film has a higher value compared to the bulk system.  $R_g$  is almost the same for all the systems. In all systems the surface area of the simulation cell is the same so we can directly compare the film thicknesses and in future we can easily backmap from the CG to AA system. The film thicknesses are influenced not only by the average bulk density but also by the density at the surfaces. In the AA system the thickness of the PS film is defined as the cell length,  $L_z$ , minus the distance from the Au atom at the bottom of the slab at  $z = 0$  nm to the Au atom at the top of the slab at 1.413 nm. The film thicknesses for all three CG potentials are only slightly smaller than the AA film thickness, and the three different CG potentials have very similar average densities and film thicknesses.

**Density Profiles.** To check that the CG systems give reasonable agreement with the AA systems, we take the S5 system and compare the structural properties. The AA density profiles are symmetrized along the  $z$ -axis. The monomer and bead density profiles are shown in Figures 6a and 6b, respectively. The monomer densities for the three CG systems are similar except that the CS-3I-P2 and CS-7I-P2 systems exhibit a double peak around 0.3–0.4 nm, whereas the M-3I-P2

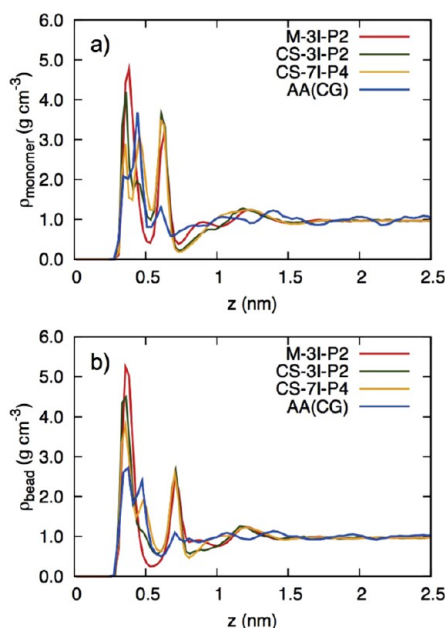


**Figure 6.** Monomer (top) and bead (bottom) density profiles for S5 films with the three CG interface potentials and the AA model (mapped to CG representation).

system has a single peak. The AA system has a shoulder in the peak at 0.4 nm. While the relative height of the double peaks for the CS-3I-P2 and CS-7I-P2 systems are different than the AA system, the positions are in good agreement. However, the CG models all predict a strong second peak at around 0.6–0.7 nm, which is very small in the AA system. The bead density profiles are similar to the monomer density profiles. The CG systems show two strong peaks at the surface compared with only one strong (double) peak and one very weak peak for the AA system. The first peak for the CG system is also rather higher than for the AA system.

To find the origin of this discrepancy, the density profiles for the individual bead types, i.e. E, P1, P2, and P3, were also calculated and are shown in Figure 7. The three CG systems and the AA system have almost identical bead density profiles for the E beads. The AA and CG profiles are very similar for P1 and P3, with the peaks in the same position but the height of the AA peaks being about half that of the CG peaks. However, for the central P beads (P2) the CG systems and the AA system are clearly different. All three CG systems have an inner peak at around 0.7 nm and additional peak (or plateau in the case of the CS-3I-P2 CG potential) around 0.3–0.5 nm. In contrast, the AA density profile for the P2 beads has a single peak at around 0.4–0.5 nm. This difference is a local effect that does not involve mass transfer toward the surface. This is clear from the density profile of the E beads, which is the same for the AA and CG systems.

The difference in the first peak or plateau of the P2 beads for the CG films is not surprising since the main difference in the potentials is between the fitting of the central P bead, as shown previously in Figure 1. To check that the appearance of the strong second peak is not due to long-range correlations missed by using an oligomer to determine the effective potentials, we performed short simulations of 100 trimers between two gold surfaces. Similarly, the CG density profiles for the central P2 beads exhibit an inner peak that does not appear in the AA density profile. The density profiles for this system are shown in the Supporting Information. The appearance of the strong second peak is likely to be a consequence of approximating the atomistic potentials by spherical CG potentials. It could also be in part due to the slightly different angular distributions between the AA and CG models.

**Bond Orientation.** The structure of the polymer–metal interfaces can be directly studied through a vector order parameter. Here, we use the bond orientation parameter  $P_2$ , which is defined as

$$P_2 = \frac{3}{2} \langle \cos^2 \theta \rangle - \frac{1}{2} \quad (4)$$

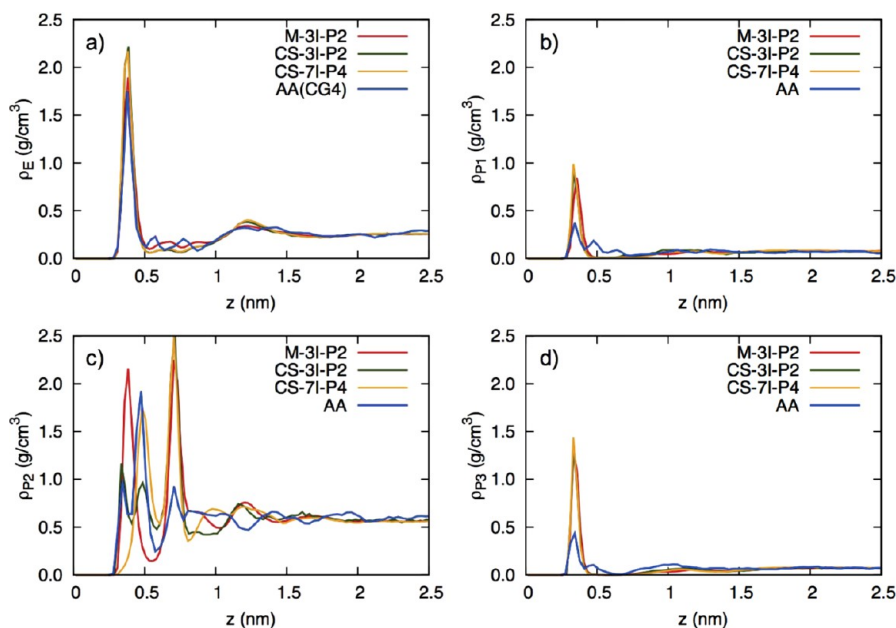


**Figure 7.** Bead density profiles for the CG and AA S5 films for each bead type (a) E, (b) first phenylene group (P1), (c) all central phenylene groups (P2), and (d) the terminal phenylene group (P3).



where  $\theta$  is the angle between the bond vector and the  $z$ -axis. We investigate the bond orientation profiles for the AA system and the three CG systems. As before, the AA system was mapped to the CG representation for analysis and the profile was symmetrized along the  $z$ -axis. First, we look at the bond orientation parameter for the vector E-P, shown in Figure 8a.

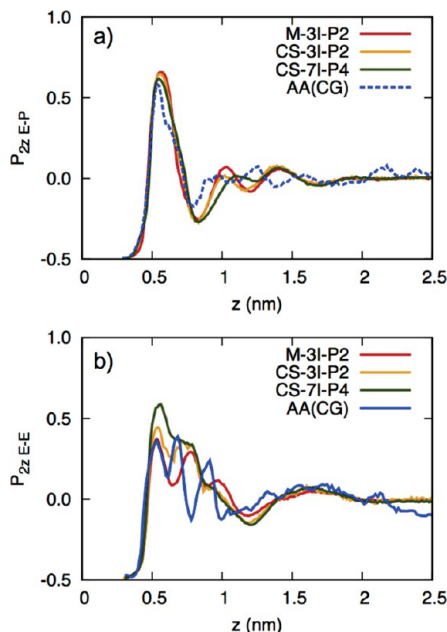


**Figure 8.** Bond orientation profiles for the S5 system using the AA and CG models. The top graph shows the bond orientation parameter for the vector E-P within the same monomer and the lower graph for the vector E-E in adjacent monomers.

As shown in our previous paper,<sup>14</sup> the bond orientation parameter next to the surface, in the first density peak at 0.3–0.4 nm, is close to  $-0.5$ , which corresponds to the vectors lying parallel to the surface. Similar behavior is seen for the bond orientation parameter E-E, which corresponds to the backbone, shown in Figure 8b. In both cases there is no significant difference between the three CG systems and the AA system.

**Chain Conformations.** The conformation of the chains in the films is compared by analyzing the conformation tensor along the  $z$ -direction with a bin size of roughly 0.5 nm. To obtain smoother curves, the results were analyzed using overlapping bins. The conformation tensor is defined as

$$C_{\alpha\beta} = 3 \frac{\langle R_{e\alpha} R_{e\beta} \rangle}{\langle R_{e,\text{bulk}}^2 \rangle} \quad (5)$$

so that for a homogeneous system the conformation tensor is equal to the identity matrix. The conformation tensor profiles perpendicular to the plane,  $C_{zz}$ , and parallel to the plane,  $C_{\text{par}} = \frac{1}{2}(C_{xx} + C_{yy})$ , are shown in 9. The AA system was mapped to the CG representation, and the resulting conformation tensor profile was symmetrized in the  $z$ -direction. The CG data are unsymmetrized. It is clear that the chains at the surface are flattened in  $z$  and elongated in the surface plane, which is typical behavior for polymers at solid surfaces. In addition, all three CG potentials give very similar conformation tensor profiles and are in excellent quantitative agreement with the AA system.

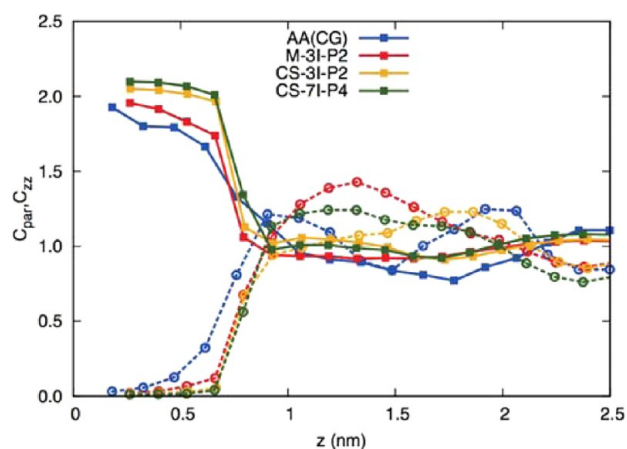


**Figure 9.** Conformation tensor profiles for the S5 system using the AA and CG models.  $C_{\text{par}}$  is shown with solid squares, and solid lines and  $C_{zz}$  is shown with open circles and dashed lines.

## COARSE-GRAINED SIMULATIONS OF LONG-CHAIN POLYSTYRENE FILMS

Overall, it is clear that there is very good agreement between the AA and CG PS/Au systems concerning the structural properties of the interfaces for all CG PS/Au interaction potentials. Now we turn to larger systems with longer polymer chains, and we have chosen to use the CS-3I-P2 potential. We consider PS films roughly 10 and 20 nm thick with 10-mer, 50-mer, 100-mer, and 200-mer chains. For the systems with longer chains the surface area of the simulation cell is increased to avoid the polymer interacting with its own periodic image. The box lengths along  $x$  and  $y$  are fixed to be a multiple of the Au surface unit cell, so that the system can be backmapped to the atomistic level, but allowed to vary in the  $z$  direction.

Equilibration of long-chain polymers is not a trivial issue. One measure of equilibration is when the end-to-end distance vectors  $R_e$  have decorrelated.<sup>27,28</sup> At 500 K this happens in less than a nanosecond for bulk 10-mer systems and around 20–30 ns for the 10-mer thin films. For longer-chain systems the time to decorrelation at 500 K is much longer, and it is necessary to heat the system until  $R_e$  is decorrelated and then cool it back to 500 K. For the 50-mer and 100-mer systems the annealing temperature was 800 K, and for the 200-mer systems the annealing temperature was 1000 K. Two different cooling rates were tested: (a)  $\Gamma = 10$  K/ns and (b)  $\Gamma = 1$  K/ns. After cooling to 500 K the systems were run for a further 100 ns before statistics were taken. No systematic dependence of the properties on cooling rate was observed. The internal distances,  $\langle R^2(N)/N \rangle$ , of each system were calculated to check that there was no residual strain in the chain. The decorrelation times and internal distances can be found in the Supporting Information. All CG simulations were NpT with  $p = 1$  atm and  $T = 500$  K and were run for 500 ns, after equilibration. Note that the time here refers to coarse-grained time, which is faster than the real or atomistic time due to the reduced friction of the smoother energy landscape.

**Average Film Properties.** The ensemble-averaged film properties are shown in Table 3. Only the data for the fast-cooled films are shown here, but the data for the slow-cooled films are given in the Supporting Information. There is no significant change in average properties between 10 and 20 nm films. For all chain lengths  $R_e$  and  $R_g$  are slightly larger in the films than in the bulk. To investigate further the differences, it



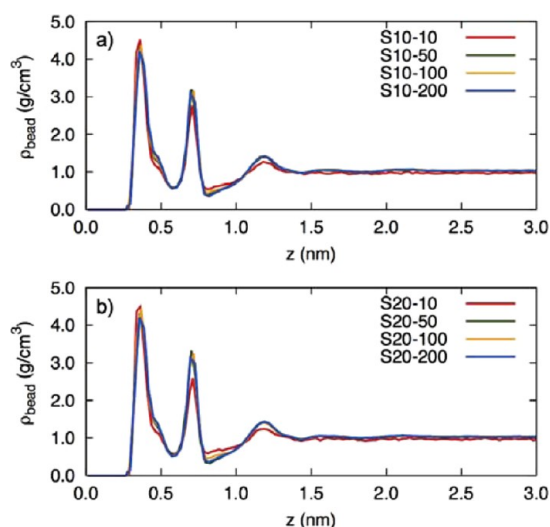
**Table 3. Summary of the CG Systems Studied and Their Averaged Properties<sup>a</sup>**

label	<i>N</i>	<i>N</i> <sub>chain</sub>	<i>L<sub>x</sub></i>	$\langle L_z \rangle$	$\langle \rho \rangle$	$\langle R_e \rangle$	$\langle R_g \rangle$
B-10	10	50		4.47	0.967	1.55	0.62
S20-10	10	200	4.616	19.34	0.969	1.58	0.62
S10-10	10	100	4.616	9.64	0.972	1.61	0.62
S5-10	10	50	4.616	4.79	0.978	1.65	0.63
B-50	50	50		7.50	1.025	3.89	1.62
S20-50	50	100	6.347	24.19	1.025	3.86	1.62
S10-50	50	50	6.347	12.10	1.024	3.92	1.64
B-100	100	50		9.42	1.033	5.61	2.38
S20-100	100	100	9.232	22.70	1.032	5.57	2.40
S10-100	100	50	9.232	11.37	1.031	5.63	2.42
B-200	200	50		11.86	1.037	8.16	3.43
S20-200	200	100	12.694	23.93	1.036	7.96	3.36
S10-200	200	50	12.694	11.98	1.034	8.19	3.48

<sup>a</sup>*N*<sub>chain</sub> is the number of chains of *N* monomers. *L<sub>x</sub>*, *L<sub>y</sub>*, *R<sub>e</sub>*, and *R<sub>g</sub>* are in nm and the average density  $\rho$  is in g cm<sup>-3</sup>. The bulk systems are in cubic boxes with *L<sub>x</sub>* = *L<sub>y</sub>* = *L<sub>z</sub>* so only  $\langle L_z \rangle$  is given. For the slabs the box is hexagonal with *L<sub>y</sub>* =  $\sqrt{3}L_x/2$ , so only *L<sub>x</sub>* (fixed) and  $\langle L_z \rangle$  are given.

is necessary to look at the various properties as a function of distance from the surface.

**Density.** The bead density profiles of the films are shown in Figure 10. For 10 and 20 nm films and all chain lengths the

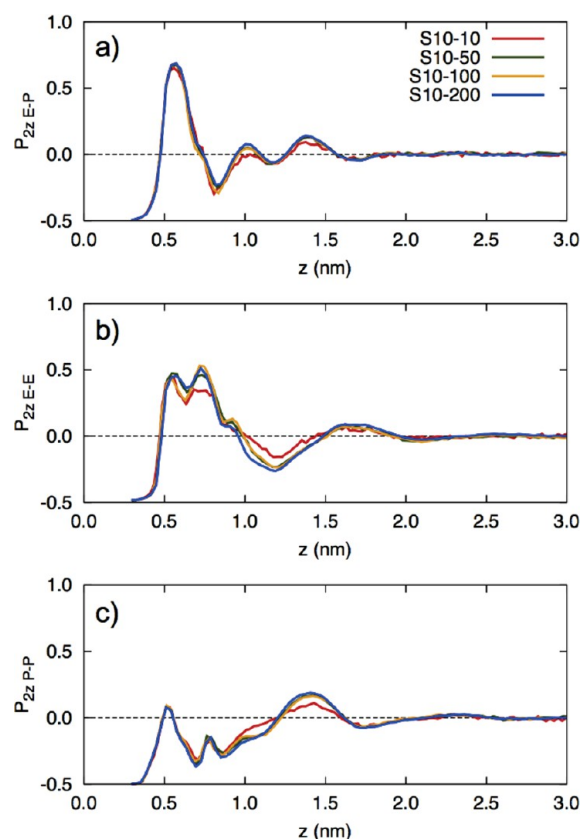
**Figure 10.** CG bead density profiles for (a) 10 nm and (b) 20 nm films.

bead density profiles are almost indistinguishable. Similar to the S5 CG systems, there are two strong peaks in the density at the surface, a weak peak at around 1.2 nm, and the profile reaches the bulk value around 1.5–2 nm.

By analyzing the partial densities for the S10 and S20 films, it is clear that the first peak is composed of both P and E beads. For the 10-mer film the contribution of P beads is higher than for the E beads, but for the 200-mer film the contributions are approximately equal. The 50-mer and 100-mer films are similar to the 200-mer film. In all films the second peak is entirely due to P beads. This implies that the backbone is lying along the surface with some P beads alongside but the other P beads forming the next density layer. However, we note that this second peak in the CG model is rather higher than for the AA

result, as discussed in the previous section. The next backbone layer occurs at around 1.2–1.3 nm from the surface. The partial density profiles for the S10-10 and S10-200 films are shown in the Supporting Information.

**Bond Orientation.** We have calculated the bond orientation profiles for four different vectors: E-P, E-E, P-E, and P-P. It is clear that at the surface, in the first density peak, the bond orientation parameters for all vectors are almost  $-0.5$ , indicating that the bonds are flat along the surface. As expected, the profiles for E-P and P-E are very similar. These profiles have a peak at around 0.5–0.6 nm, which implies a tendency for the bonds to be perpendicular to the surface, and then are approximately 0 after 1.5 nm. The E-E bond vector has a slightly lower but broader peak at 0.5–0.7 nm. These peaks correspond to the density minima at 0.5 nm (see Figure 10), and therefore, this reflects the bonds connecting E beads in the first layer with P beads in the second layer. The P-P bond orientation parameter profile is qualitatively different to the other vectors and does not have a peak at 0.5 nm. Instead, it approaches 0 at around 0.5 nm, indicating random orientation, becomes negative again, indicating a weak preference for parallel orientation, and becomes approximately random again after 1.5 nm.

**Figure 11.** Bond orientation parameter profiles for the vectors (a) E-P, (b) E-E, and (c) P-P.

**Conformation Tensor.** To analyze the conformation tensor, the average mean square end-to-end distance ( $\langle R_e^2 \rangle$ ) of the two bulk runs (with different cooling rates) was used. As before, the parallel component has been averaged over the *xx* and *yy* components:  $C_{\text{par}} = 1/2(C_{xx} + C_{yy})$ . To obtain smoother curves, the profiles were plotted using overlapping bins of

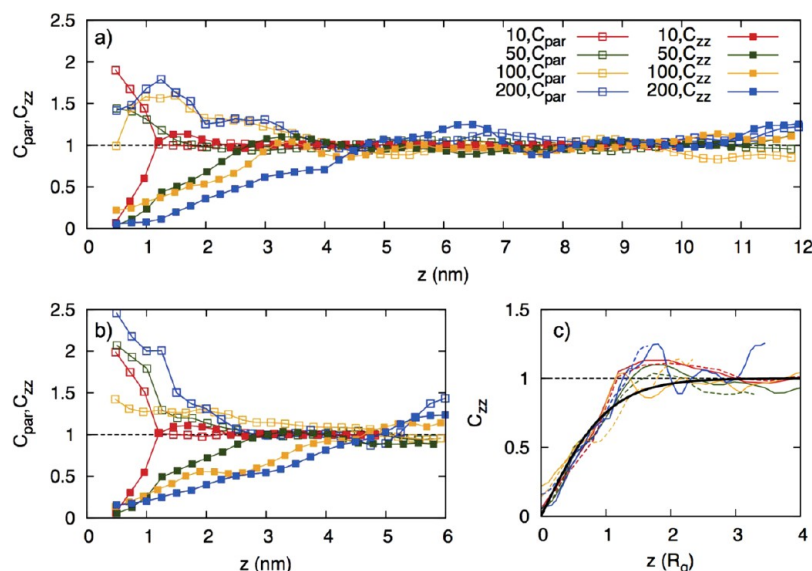


**Figure 12.** Conformation tensor profiles for (a) 20 nm films, (b) 10 nm files, and (c) all films plotted in reduced units of  $R_g$ . The key is the same for (a) and (b). In (c) the 20 nm films are plotted using solid lines and the 10 nm films using dashed lines, with the color code the same as in (a). The black line is the hyperbolic tangent that is the best fit to all the data.

roughly 0.5 nm and the conformation tensor profiles were symmetrized. The profiles are shown in Figure 12.

It is clear from Figure 12a,b that in all films the chains nearest the surfaces are lying parallel to the  $z$ -direction. The in-plane component of the tensor is rather noisier and shows a much larger fluctuation near the surface. In particular, in the S20-100 system the value at the surface is close to 1.0, which is considerably lower than the other films. This noise is due to the fact that the films are quite immobile near the surface and, in addition, the 100- and 200-mer chains in bulk do not fully decorrelate within 500 ns at 500 K and are likely to be dependent on the setup. To check if this is the case, an independent S20-100 system was set up for both cooling rates and the conformation tensor  $C_{\text{par}}$  had values of 2.7 and 3.6 at the surface for the fast and slow cooling rates, respectively, which is within the statistical error bars. The data for all cooling rates and systems are given in the Supporting Information.

To further analyze the conformation tensor, the  $C_{zz}$  profiles were plotted in terms of reduced units, as shown in Figure 12c. We chose to analyze  $C_{zz}$  since they are less noisy than the  $C_{\text{par}}$  profiles. It is clear that all the profiles map onto a master curve, with a small peak around  $1-2R_g$ .

**Interphase Width.** It is well-known that the interphase width is nonunique and is property specific. From the above analysis we can estimate the width of the interphase,  $W$ , and its dependence on chain length.

The density profiles for all films are almost identical and reach a bulk value at around  $W_\rho = 1.5$  nm, which is independent of chain length. This is similar to the value of 1–2 nm that was observed previously in studies of 10-mer PS on silica nanoparticles<sup>29</sup> and 80-mer PS on a nonspecific surface.<sup>9</sup> The bond orientation parameters become random at around  $W_{Pz} = 1.5$  nm, which is also independent of chain length. Clearly, since these are segmental quantities, the interphase width measured in this way is independent of the chain length.

However, the distance at which the conformation tensor profile reaches its bulk behavior is not chain length independent, as is shown in Figure 12. In order to estimate

the interphase width, the conformation tensor profiles  $C_{zz}$  were fitted using hyperbolic tangents of the form

$$C_{zz}(z) = \tanh(z/A)$$

To improve statistics all data for both 10 and 20 nm films and both cooling rates were fitted (16 curves in total), and further details of the fitting procedure are given in the Supporting Information. For each profile the fitting parameter  $A$  was calculated, and the average value for all the data is  $A = 1.023$  in units of  $R_g$ , and this curve is plotted as the black solid line in Figure 12c. This curve approaches  $C_{zz} = 1$  asymptotically, but we can estimate a range for the interphase width of around  $2-3R_g$ . The interphase width estimate is plotted in Figure 13. For comparison, we have plotted  $R_g$  and  $R_e$  for the bulk systems. The lines show the fits to the data of the form

$$R_{e/g} = kN^{1/2}$$

and it is clear that  $R_g$  and  $R_e$  vary with  $N$ . The estimated interphase width of  $2-3R_g$  closely follows  $R_e$ . This is similar to

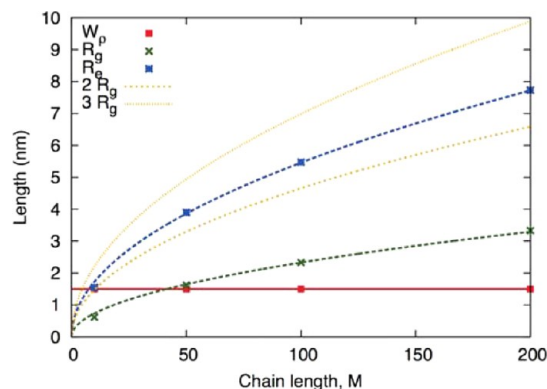


**Figure 13.** Dependence of estimated interphase width on chain length using density profiles, and conformation tensor profiles. For comparison,  $R_g$  and  $R_e$  for the bulk systems are also plotted. The dashed lines are fits to the data of the form  $kN^{1/2}$ .

the value found in studies of polyethylene on graphite,<sup>30</sup> polyamide-6,6 on graphene,<sup>31</sup> and slightly larger than for polypropylene on graphite.<sup>32</sup> A previous study using a generic CG model analyzed the components of  $R_g$  and found that they reached the bulk value after a distance of  $R_g$  from the surface.<sup>33</sup>

## SUMMARY AND CONCLUSIONS

A coarse-grained model for polystyrene on a gold surface was developed and used to investigate the structure of polystyrene films confined between parallel gold surfaces. The method used a hierarchical multiscale modeling approach where the surface interaction is based on density functional theory calculations and all-atom molecular dynamics simulations. The interface potentials were validated by comparing the coarse-grained and all-atom structures of a 5 nm thick 10-mer polystyrene film on gold. The density and conformational properties using the all-atom and coarse-grained model were found to be in good agreement.

The structural properties of 10-mer to 200-mer polystyrene films roughly 10 and 20 nm thick confined between gold surfaces were then investigated using the coarse-grained model. The density profile at the interface was analyzed, and it was found that both film thickness and all chain lengths gave almost indistinguishable profiles. The density reached the bulk value at around 1.5 nm from the surface. The conformation of the films was also analyzed, and the distance from the interface where the bulk value was reached was found to be proportional to the square root of the chain length and roughly 2–3 times the radius of gyration. For 200-mer chains, the longest chain length studied here, the interphase width is estimated to be between 6 and 10 nm, which is similar to the average end-to-end distance. Clearly, the interphase width and its variation with chain length depend on the property that is measured. The width of the interphase based on polymer dynamics should also be investigated, but this is a topic for a future article.

## ASSOCIATED CONTENT

### Supporting Information

The supporting information clarifies the mapping scheme and discusses in more detail the differences in the density profiles between the AA and CG systems. The equilibration of long chain polymers melts is described and a table with the average properties of all the systems is presented. Additional graphs for partial densities and an explanation of the fitting of the conformation tensor profiles are also provided. This material is available free of charge via the Internet at <http://pubs.acs.org>.

## AUTHOR INFORMATION

### Corresponding Author

\*E-mail: [johnston@mpip-mainz.mpg.de](mailto:johnston@mpip-mainz.mpg.de) (K.J.).

### Notes

The authors declare no competing financial interest.

## ACKNOWLEDGMENTS

We thank Sebastian Fritsch and Dominik Fritz for valuable help and Kurt Kremer and Christine Peter for useful discussions and critical reading of the manuscript. This work was supported by the German Research Foundation (DFG) grant SPP 1369 "Interfaces and interphases". This work was partially supported by the European Union's Seventh Framework Programme (FP7-REGPOT-2009-1) project "Archimedes Center for Modeling, Analysis and Computation".

## ADDITIONAL NOTE

<sup>a</sup>In the previous publication<sup>14</sup> the system was labeled S3, but in this paper we change the notation to S5-10, denoting the approximate film width and the number of monomers per chain.

## REFERENCES

- (1) Koo, J. *Polymer Nanocomposites: Processing, Characterization, And Applications*; McGraw-Hill: New York, 2006.
- (2) Kim, H.; Abdala, A. A.; Macosko, C. W. *Macromolecules* **2010**, *43*, 6515.
- (3) Priestley, R. D.; Ellison, C. J.; Broadbelt, L. J.; Torkelson, J. M. *Science* **2005**, *309*, 456.
- (4) Qi, D.; Fakhraei, Z.; Forrest, J. A. *Phys. Rev. Lett.* **2008**, *101*, 096101.
- (5) Tress, M.; Erber, M.; Mapesa, E. U.; Huth, H.; Mueller, J.; Serghei, A.; Schick, C.; Eichhorn, K.-J.; Voit, B.; Kremer, F. *Macromolecules* **2010**, *43*, 9937.
- (6) Hoppe, E. T.; Hopp, I.; Port, M.; Menges, B.; Papadakis, C. M. *Colloid Polym. Sci.* **2012**, *290*, 1731.
- (7) Doi, M.; Edwards, S. F. *The Theory of Polymer Dynamics*; Clarendon Press: Oxford, England, 1986.
- (8) Borodin, O.; Smith, G. D.; Bandyopadhyaya, R.; Bytner, O. *Macromolecules* **2003**, *36*, 7873.
- (9) Hudzinsky, D.; Lyulin, A. V.; Baljon, A. R. C.; Balabaev, N. K.; Michels, M. A. J. *Macromolecules* **2011**, *44*, 2299.
- (10) Yelash, L.; Virnau, P.; Binder, K.; Paul, W. *Europhys. Lett.* **2012**, *98*, 28006.
- (11) Harmandaris, V. A.; Daoulas, K. C.; Mavrantzas, V. G. *Macromolecules* **2005**, *38*, 5796.
- (12) Eslami, H.; Müller-Plathe, F. *J. Phys. Chem. B* **2009**, *113*, 5568.
- (13) Yelash, L.; Virnau, P.; Binder, K.; Paul, W. *Phys. Rev. E* **2010**, *82*, 050801.
- (14) Johnston, K.; Harmandaris, V. *Soft Matter* **2012**, *8*, 6320–6332.
- (15) Abrams, C. F.; Kremer, K. *Macromolecules* **2003**, *36*, 260.
- (16) Villa, A.; Peter, C.; van der Vegt, N. F. A. *Phys. Chem. Chem. Phys.* **2009**, *11*, 2077.
- (17) Fritz, D.; Harmandaris, V. A.; Kremer, K.; van der Vegt, N. F. A. *Macromolecules* **2009**, *42*, 7579.
- (18) Fritz, D.; Koschke, K.; Harmandaris, V. A.; van der Vegt, N. F. A.; Kremer, K. *Phys. Chem. Chem. Phys.* **2011**, *13*, 10412.
- (19) Delle Site, L.; Abrams, C. F.; Alavi, A.; Kremer, K. *Phys. Rev. Lett.* **2002**, *89*, 156103.
- (20) Johnston, K.; Nieminen, R. M.; Kremer, K. *Soft Matter* **2011**, *7*, 6457–6466.
- (21) Johnston, K.; Harmandaris, V. *J. Phys. Chem. C* **2011**, *115*, 14707.
- (22) Hess, B.; Kutzner, C.; van der Spoel, D.; Lindahl, E. *J. Chem. Theory Comput.* **2008**, *4*, 435–447.
- (23) Müller-Plathe, F. *Macromolecules* **1996**, *29*, 4782.
- (24) Harmandaris, V. A.; Reith, D.; van der Vegt, N. F. A.; Kremer, K. *Macromol. Chem. Phys.* **2007**, *208*, 2109.
- (25) Bussi, G.; Donadio, D.; Parrinello, M. *J. Chem. Phys.* **2007**, *126*, 014101.
- (26) Bochkhanov, S.; Bystritsky, V. *ALGLIB*; <http://www.alglib.net/>.
- (27) Mavrantzas, V. G.; Boone, T. D.; Zervopoulou, E.; Theodorou, D. N. *Macromolecules* **1999**, *32*, 5072.
- (28) Auhl, R.; Everaers, R.; Grest, G. S.; Kremer, K.; Plimpton, S. J. *J. Chem. Phys.* **2003**, *119*, 12718.
- (29) Ndo, T. V. M.; Voyiatzis, E.; Ghanbari, A.; Theodorou, D. N.; Böhm, M. C.; Müller-Plathe, F. *Macromolecules* **2011**, *44*, 2316.
- (30) Daoulas, K. C.; Harmandaris, V. A.; Mavrantzas, V. G. *Macromolecules* **2005**, *38*, 5780.
- (31) Eslami, H.; Müller-Plathe, F. *J. Phys. Chem. C* **2013**, *117*, 5249.
- (32) Mansfield, K. F.; Theodorou, D. N. *Macromolecules* **1991**, *24*, 4295.
- (33) Virgilis, A. D.; Milchev, A.; Rostiashvili, V. G.; Vilgis, T. A. *Eur. Phys. J. E* **2012**, *35*, 97.